Monthly Notices of the ROYAL ASTRONOMICAL SOCIETY

MNRAS **528,** 2511–2522 (2024) https://doi.org/10.1093/mnras/stae169
Advance Access publication 2024 January 16

MIGHTEE polarization early science fields: the deep polarized sky

A. R. Taylor [1,2,3★] S. Sekhar [1,2,3,4★] L. Heino,[1,2] A. M. M. Scaife [5,6] J. Stil,[7] M. Bowles,[5] M. Jarvis [8] I. Heywood[8,9,10] and J. D. Collier[1,2,11]

[1]*Inter-University Institute for Data Intensive Astronomy, Univrsity of Cape Town, Rondebosch, 7701, South Africa*
[2]*Department of Astronomy, University of Cape Town, Rondebosch, Cape Town, 7701, South Africa*
[3]*Department of Physics and Astronomy, University of the Western Cape, Bellville, Cape Town, 7535 South Africa*
[4]*National Radio Astronomy Observatory, Socorro, NM, 878010-0387, USA*
[5]*Department of Physics and Astronomy, University of Manchester, Manchester, M13 9PL, UK*
[6]*The Alan Turing Institute, Euston Road, London NW1 2DB, UK*
[7]*Department of Physics and Astronomy, University of Calgary, Calgary, T2N 1N4, Canada*
[8]*Department of Astrophysics, University of Oxford, Oxford, 0X1 3PU, UK*
[9]*Centre for Radio Astronomy Techniques and Technologies, Department of Physics and Electronics, Rhodes University, Makhanda, 6139, South Africa*
[10]*South African Radio Astronomy Observatory, Observatory, 7925, Cape Town, South Africa*
[11]*School of Science, Western Sydney University, Locked Bag 1797, Penrith, NSW 2751, Australia*

Accepted 2023 December 21. Received 2023 December 19; in original form 2023 November 1

ABSTRACT

The MeerKAT International GigaHertz Tiered Extragalactic Exploration (MIGHTEE) is one of the MeerKAT large survey projects, designed to pathfind SKA key science. MIGHTEE is undertaking deep radio imaging of four well-observed fields (COSMOS, *XMM*-LSS, ELAIS S1, and CDFS) totaling 20 square degrees to μJy sensitivities. Broad-band imaging observations between 880 and1690 MHz yield total intensity continuum, spectro-polarimetry, and atomic hydrogen spectral imaging. Early science data from MIGHTEE are being released from initial observations of COSMOS and *XMM*–LSS. This paper describes the spectro-polarimetric observations, the polarization data processing of the MIGHTEE early science fields, and presents polarization data images and catalogues. The catalogues include radio spectral index, redshift information, and Faraday rotation measure synthesis results for 13 267 total intensity radio sources down to a polarized intensity detection limit of $\sim$20 μJy bm^{-1}. Polarized signals were detected from 324 sources. For the polarized detections, we include a catalogue of Faraday Depth from both Faraday Synthesis and Q, U fitting, as well as total intensity and polarization spectral indices. The distribution of redshift of the total radio sources and detected polarized sources are the same, with median redshifts of 0.86 and 0.82, respectively. Depolarization of the emission at longer-wavelengths is seen to increase with decreasing total-intensity spectral index, implying that depolarization is intrinsic to the radio sources. No evidence is seen for a redshift dependence of the variance of Faraday depth.

Key words: instrumentation: interferometers – polarization – techniques: polarimetric – surveys – radio continuum: galaxies.

1 INTRODUCTION

The MeerKAT telescope is the precursor of the Square Kilometre Array mid-frequency dish array to begin deployment later this decade on the Karroo Plateau in South Africa. The MeerKAT MIGHTEE survey (Jarvis et al. 2016) is undertaking deep radio imaging of four extragalactic fields, COSMOS, *XMM*-LSS, CDFS, and ELAIS S1. All fields are being observed at L band from 880–1680 MHz, in multiple pointings that will be mosaiced to a final image with a broad-band sensitivity of $\sim$2 μJy beam^{-1}. The MIGHTEE project is creating science data products for total intensity, broad-band continuum science, H I spectral line science, and spectropolarimetric science, to explore dark matter, large-scale structure, and the evolution of galaxies.

Radio polarimetry is a powerful probe of cosmic magnetic fields, and is central to science programs on next generation radio facilities and to planning for the Square Kilometre Array (Heald et al. 2020). Deep polarization imaging offers the potential to explore cosmic magnetism to flux density levels where the radio population transitions from AGN-dominated to star formation galaxies at intermediate redshifts (Taylor et al. 2015).

The MIGHTEE project is releasing data for early science from initial observations of portions of the COSMOS and *XMM*-LSS regions. Early science total intensity images and catalogues were released by Heywood et al. (2022). This document describes the spectropolarimetric data processing and early science polarization data products.

★ E-mail: russ@idia.ac.za (ART); srikrishna@idia.ac.za (SS)

Table 1. Observations for the MIGHTEE-pol Early Science Release.

Pointing	Date	Time (h)	N antennas
XMMLSS_12	2018-10-06	8.02	59
XMMLSS_12	2018-10-11	8.05	63
XMMLSS_13	2018-10-07	8.07	59
XMMLSS_13	2018-10-12	8.03	62
XMMLSS_14	2018-10-08	8.03	60
XMMLSS_14	2018-10-13	8.00	62
COSMOS	2018-04-19	8.65	64
COSMOS	2018-05-06	8.39	62
COSMOS	2020-04-26	7.98	59

2 OBSERVATIONS

MeerKAT is an array of 64, 13.5-m diameter radio antennas located in the Karroo Plateau in South Africa (Jonas & MeerKAT Team 2016). The MIGHTEE early science observation consist of one pointing centred on the COSMOS field and three adjacent overlapping pointings in *XMM*-LSS labelled XMMLSS_12, XMMLSS_13, XMMLSS_14. Each of the pointing centres for the *XMM*-LSS were observed twice with MeerKAT for approximately 8 h. For the COSMOS pointing three 8-h observations were obtained. Table 1 summarizes the observations. The number of antennas participating in an observation ranged from a minimum of 59 to a maximum of the full array of 64.

For the XMMLSS pointings, J1939−6342 was used as the primary calibrator for calibration of the flux density scale and complex bandpass. Time-dependent gain was tracked by observation of the secondary calibrator J0201−-1132 every 20 to 30 min during the 8 h track. The polarized source J0521+1638 (3C138) was used for absolute polarization angle and observed once or twice during a track. For COSMOS the primary was J0408−6565, the secondary was J1008+0740, and J1331+3030 (3C286) was used for polarization angle. Observations taken in 2018 used the 4096 channel coreeeeeaaarelator mode. The observation of COSMOS in 2020 was taken with 32 768 channels. In that case the visibility data were averaged to 4096 channels before processing.

3 DATA PROCESSING

The visibility data were calibrated and imaged in full polarization mode on the ilifu cloud facility using the CASA-based IDIA pipeline.[1] The pipeline partitions the *L*-band RF into 15 spectral windows between 880 and 1680 MHz. Data in frequency ranges with strong persistent RFI (933–960, 1163–1299, and 1525–1630 MHz) are removed at this partition stage. Fig. 1 shows a sample plot of the time averaged visibility amplitudes on J1939−6342, and illustrates the regions removed due to RFI.

Each of the 14 spectral windows is split into its own multimeasurement set (MMS) that is processed concurrently using the ilifu SLURM job manager. Following calibration the calibrated data from each spectral window is merged into a single measurement set (MS) with calibrated visibilities.

For ideal linear feeds, the linear approximation to the response of the parallel and cross hand visibilities is given by the equations (1)–(4) below. In these equations, we have retained only the first-order leakage terms (i.e. those leakage terms that multiply Stokes *I*). A more complete set including leakage terms that multiply the source polarization can be found in Hales (2017).

[1] https://idia-pipelines.github.io/docs/processMeerKAT

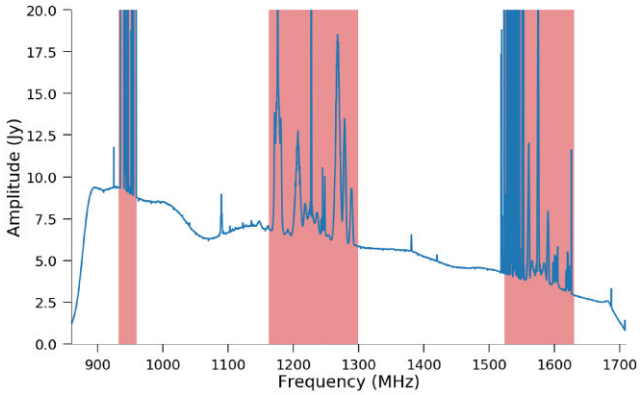

Figure 1. Plot of the MeerKAT time-averaged bandpass response on J1939−6342. The regions highlighted in red have strong, persistent RFI in all observations and are removed for all data sets.

$$V_{xx} = g_x^i g_x^k \left(I + Q\cos 2\psi + U \sin 2\psi\right) \quad (1)$$

$$V_{xy} = g_x^i g_y^k \left[(d_x^i - d_y^{k\,*})I - Q \sin 2\psi + U \cos 2\psi + jV\right] \quad (2)$$

$$V_{yx} = g_y^i g_x^k \left[(d_x^{k\,*} - d_y^i)I - Q \sin 2\psi + U \cos 2\psi - jV\right] \quad (3)$$

$$V_{yy} = g_y^i g_y^k \left(I - Q\cos 2\psi - U \sin 2\psi\right) \quad (4)$$

Any polarized signal from the source is present in all four correlations and varies with parallactic angle ψ. Consequently, the source polarization signal affects both the gain solutions and the leakage. The accuracy of the Stokes Q response ($V_{xx} - V_{yy}$) is dependent on the knowledge of the complex gains g_x and g_y. Precise measurement of the gains and the leakage terms can be achieved using a strong unpolarized source for which the equations reduce to

$$V_{xx} = g_x^i g_x^k I \quad (5)$$

$$V_{xy} = g_x^i g_y^k (d_x^i - d_y^{k\,*})I \quad (6)$$

$$V_{yx} = g_y^i g_x^k (d_x^{k\,*} - d_y^i)I \quad (7)$$

$$V_{yy} = g_y^i g_y^k I \quad (8)$$

These equations cleanly separate the gain solution into the parallel-hand correlations and the gain leakage into the cross-hand correlations.

Prior to calibration, the data are first flagged to eliminate the frequency windows that contain persistent RFI, as shown in Fig. 1.

Following automated flagging, as a first step in the calibration we use the observations of the primary calibrator to measure the frequency-dependent g_x and g_y gains using an absolute flux bandpass solution. Assuming the primary calibrators are unpolarized (but see Section 4.2), we apply the frequency-dependent gain solutions and derive the leakage terms also using the primary.

The secondary calibrator is used to calculate polarization-independent, but time-dependent, residual complex gains. The XX and YY signals were averaged (`gaintype = 'T'` in CASA task `gaincal`) so any polarization of the secondary does not modify the relative X, Y gains derived from the primary. Finally, the scan on the polarization calibrator (one of either J0521+1638 or J1331+3030) was used for absolute X–Y phase calibration. We find that the XY

Table 2. Image and cube properties.

Pointing	Coordinates RA	Dec.	MFS image resolution (robust = −0.50)		RM Synthesis (smoothed cube) RMTF FWHM (rad m^{-2})	Median RM Synth RMS off-source (μJy beam^{-1})	Median per-chan bkgd RMS (μJy beam^{-1}) Q	U	V
XMMLSS_12	02 17 51.0	−04 59 59	7.75″ × 6.81″	−35.1°	56.8	3.12	25.3	26.9	25.1
XMMLSS_13	02 20 42.0	−04 49 59	7.69″ × 6.73″	−21.2°	56.8	3.97	27.9	31.2	27.2
XMMLSS_14	02 23 22.0	−04 49 59	7.93″ × 6.90″	−35.2°	57.6	2.90	25.3	26.1	25.4
COSMOS	10 00 28.6	+ 02 12 21	7.80″ × 7.22″	−20.1°	55.2	3.21	31.2	31.6	31.5

phase solutions are very consistent across all the early science fields, so we fit the median XY phase spectrum with a 3rd degree polynomial and apply the fitted calibration solutions. This results in more stable and smoother Q & U spectra on the calibrator and target sources.

This first round of calibration is followed by a second round of automated flagging, using the `tfcrop` and `rflag` algorithms within the CASA `flagdata` task. The flagging is carried out on the calibrated data in order to identify low-level RFI in the data. The calibration solutions are then cleared out and the entire calibration process is run again, as described above, resulting in the final calibrated measurement sets.

Following *a priori* calibration, the calibrated visibilities are self-calibrated (again using `gaintype = 'T'` to preserve the relative X,Y gains). Two self-calibration cycles are run, first calibrating only for phase, followed by a phase and amplitude solve. The self-calibrated target visibilities and calibrator visibilities are moved to the mightee-pol visibility repository on ilifu, along with all calibration tables.

Spectro-polarimetric (I, Q, U, V) hypercubes are created from the calibrated visibilities for the calibrators and the self-calibrated visibilities of the target fields using the IDIA cube generation pipeline.[2] In addition multiterm multifrequency synthesis (MT-MFS; Rau & Cornwell 2011) broad-band images are created in full Stokes. All images were constructed for each field using CASA `tclean` with the combined visibilities from the multiple observations. Image products created for each field include:

(i) Two MT-MFS broad-band I, Q, U, V images with Briggs' robust weighting (Briggs 1995) of −0.5 and +0.4. The central frequency of the images is 1.280 GHz.

(ii) Spectropolarimetric I, Q, U, V hypercubes with a Briggs' robust weighting of +0.0. Two hypercubes are constructed. For one, each frequency plane has the native resolution of the associated frequency. A second hypercube is generated with each frequency channel smoothed in the image plane to a common resolution of 18 arcsec.

For all image data the clean deconvolution is carried out with images of the entire primary beam with frame dimensions of 6144 × 6144 pixels and 1.5 arcsec cell size. For science use, the frames are reduced to 4600 × 4600 after deconvolution, yielding an image diameter of 1.92°. Table 2 lists the central coordinates of the four image sets and the restoring beams of the MFS images at robust = −0.5. The rms noise of the Stokes I plane of the MFS images, measured in a source free region far from the image centre is typically between 3 and 3.5 μJy bm^{-1}. As an example, Fig. 2 shows the distribution of pixel amplitudes in the rms image for XMMLSS_12 created with pyBDSF. The most probable value of the rms is 3.15 μJy bm^{-1} and the median value is 3.49 μJy bm^{-1}.

[2] https://github.com/idia-astro/frocc

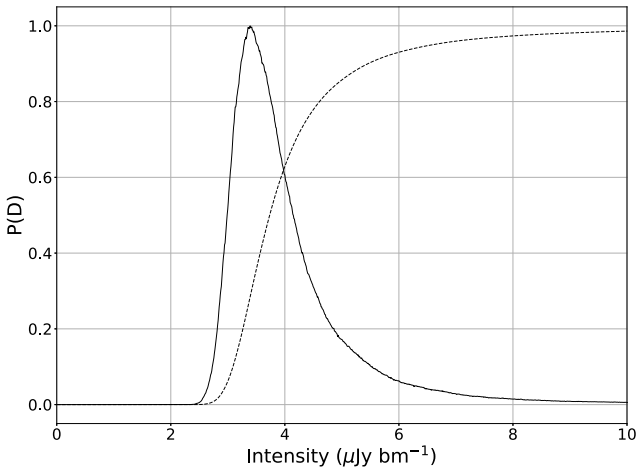

Figure 2. Distribution of pixel amplitudes (solid line) in the pyBDSF rms image for XMMLSS_12. The most probable value (distribution peak) is 3.15 μJy bm^{-1}. The median value is 3.49 μJy bm^{-1}. The dashed line shows the cumulative distribution.

The cubes span a frequency range of 794 MHz (886–1680 MHz) with channel width of 2.51 MHz. Channel images are constructed using all frequency channels within each 2.51 MHz band with CASA `tclean` in multifrequency synthesis mode (`specmode = 'mfs'`) and the w-projection gridder with 768 w planes. Channel image frames within the three frequency ranges removed due to the presence of strong, persistent interference are replaced with NaNs. The frequency ranges of contiguous good data are 887–993, 960–1163, 1299–1524, and 1630–1680 MHz, totalling 585 MHz, or 74 per cent of the band.

The MT-MFS broad-band Q, U images are provided for high-sensitivity and higher angular resolution polarization images. However a significant Faraday depth will depolarize the broad-band signals. The typical Faraday depth of the polarized sources (Fig. 8) is much less than the FWHM of the RM transfer function (Fig. 4), so most sources are detected in the MT-MFS images, if somewhat attenuated. Reference should be made to the observed Faraday depth of a source when interpreting the MT-MFS Q, U values.

4 SOURCE POLARIZATION

4.1 Spectropolarimetry

The official total intensity continuum images and catalogues for the MIGHTEE early science fields are created by the MIGHTEE continuum working group. These results have recently been published by Heywood et al. (2022). For the purpose of measuring the polarization properties of the radio sources, a total intensity source catalogue was

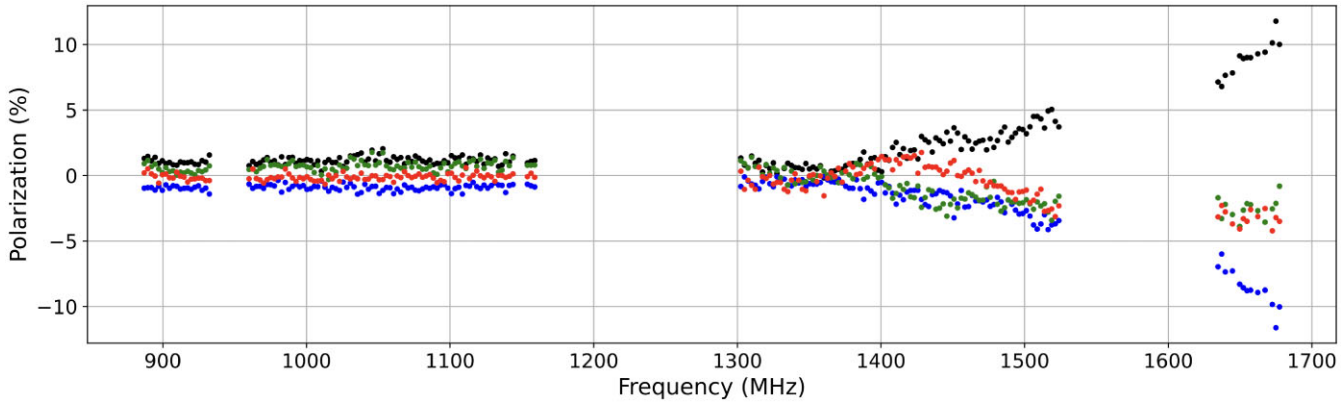

Figure 3. Percent polarization in Q, U, V (blue, green, red) and total linear polarization (black) for a strong source in XMMLSS_13 at a distance of 0.45° from the field centre. The high circular and linear polarization leakage above about 1400 MHz for this off-axis sources arises from the large differential $X - Y$ beam squint above this frequency (Asad et al. 2021; Sekhar et al. 2022).

generated for each pointing using pyBDSF on the Stokes I plane of the broad-band MFS images with robust $= -0.5$.

Spectropolarimetric data is derived for all sources within 0.5° of the image centre (approximately the half-power point of the primary beam at band centre). For each radio source, we extracted the I, Q, U, V spectral profiles at the nearest pixel to the source position in the smoothed cube. The 18 arcsec synthesized beam is heavily oversampled (12 pixels per FWHM), so the amplitude of the nearest pixel to the source position accurately represents the peak intensities.

The image cubes contain low-level, diffuse polarized signals arising from differential Faraday rotation of the Galactic synchrotron background. To remove this effect from the compact source spectra, background spectra ($Q_{\rm bkgd}$, $U_{\rm bkgd}$) were derived for each source from the average U and Q signal in an annular box around the source in each frequency channel. The width of the annulus is 26 pixels (39 arcsec). The half-width of central hole is $\Delta = 4\,\theta_s$, where θ_s is the semimajor axis of the source from the pyBDSF fit in the MFS image. The area of the annular box is ∼39 beam solid angles. The standard deviation of the values in the background box was used as an estimate of the local rms per channel around the source. The median per-channel background RMS before over all sources and channels before primary beam correction is given for Q, U, and V in Table 2. The per-channel RMS is typically 25–30 μJy beam^{-1}, and the Q and U values agree to within 4 per cent, except for XMMLSS_13 where the difference is ∼10 per cent. XMMLSS_13 is more affected by a strong, off-axis source that appears to affect the background RMS in U slightly more than Q.

4.2 Polarization leakage

On-axis leakage residuals after calibration are measured to be about 0.1 per cent. However, there is frequency-dependent beam squint and squash at the high-end of the L band (Asad et al. 2021; Sekhar et al. 2022), that leads to off-axis frequency-dependent leakage. The differential squint between the beams creates instrumental polarization that grows to levels of several per cent at the high end of the band. This effect is demonstrated in Fig. 3 which shows the per cent polarization in Q, U, and V for a strong source (13 mJy) at a distance of 0.45° from the field centre in XMMLSS_13. Above about 1400 MHz the polarization grows quickly with frequency to several per cent in all polarizations. To avoid the strong leakage at the upper end of the band we restrict the analysis the polarization signals to frequencies below 1380 MHz. Below this frequency the leakage remains less than 0.2 per cent within 0.5° of field centre.

4.3 Detection of polarized emission

To search for significant polarized emission from the radio sources, Faraday depth spectra were constructed from the background-corrected Stokes spectra of each total intensity source, as well as for one nearby off-source position that is offset from the source by Δ. The source density in the total intensity image is quite high. Care was taken to ensure that the off-source position did not coincide with a source that has total flux density greater than 100 μJy bm^{-1}. The Faraday depth spectrum is calculated as

$$F(\phi) = \left(\frac{1}{\sum_{j=1}^{N} w_j}\right) \sum_{j=1}^{N} P_j e^{-2i\phi(\lambda_j^2 - \bar{\lambda}^2)} \cdot w_j. \quad (9)$$

Here, the sum is over all channels, j, $\bar{\lambda}$ is the mean wavelength and

$$P_j = (Q - Q_{\rm bkgd})_j - i(U - U_{\rm bkgd})_j. \quad (10)$$

The RM synthesis weights are

$$w_j = \left(\frac{1}{\sigma_{QU_j}}\right)^2, \quad (11)$$

where σ_{QU_j} is the average of the Q and U local background RMS in channel j.

Faraday depth spectra were constructed, using data at frequencies less than 1380 MHz, over a Faraday depth range of ±2000 rad m^{-2}. Fig. 4 shows a characteristic RM transfer function. The missing frequency range from 1163–1299 Mhz results in strong sidelobes of about 40 per cent at an offset of about ±90 rad m^{-2} from the main lobe. The main lobe of the transfer function has a typical width of 56 rad m^{-2}. Precise values of the FWHM of the RM transfer function are given for each field in Table 2. With a channel width of 2.51 MHz, the maximum detectable rotation measure (RM) is about 5000 rad m^{-2} at band centre. For a maximum frequency of 1380 MHz, the largest detectable width for a contiguous Faraday depth feature is 67 rad m^{-2}. The noise in the RM synthesis spectrum was estimated from standard deviation of the real part of the off-source spectrum. Table 2 lists the median off source RMS over all sources for each field. The typical value is ∼3 μJy bm^{-1}, consistent with the RMS of the total intensity images.

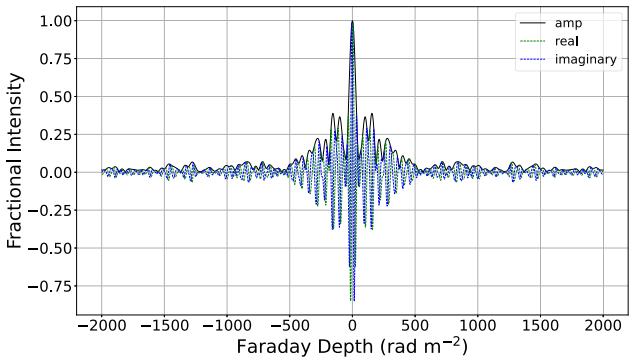

Figure 4. Typical RM transfer function for frequencies from 887 to 1380 MHz. The solid black line is the amplitude. The missing sections of the band result in high sidelobes of about 40 per cent.

The polarized intensity and Faraday depth of the strongest component in both the on-source and off-source spectra was measured for each source. The distribution of the amplitudes of the off-source spectra provides a statistical measure of the probability of detecting an RM synthesis peak of a given amplitude from the noise of the Stokes Q and U planes of the image cubes. Figs 5 and 6 show the distribution of the peak amplitude of the RM synthesis spectra for the on- and off-source positions plotted against the peak total intensity for each source. The black horizontal line in each figure is the 99.9 percentile of the off-source spectral peaks. On-source peaks (blue dots) that fall above this line are taken to be detected polarization signals. Table 3 lists the total number of total intensity sources with 0.5° of field centre, the polarization detection thresholds and the raw number of detected polarization signals for each of MIGHTEE early science fields.

The three fields observed in XMMLSS have significant overlap. We thus created a merged catalogue in which duplicate detections are removed. For objects detected in more than one field, we retained only the instance from the field in which the sources is closest to the field centre. The merged XMMLSS catalogue has 9431 total intensity radio components. Despite the local background removal (equation 10), the XMMLSS results remain affected at low flux density by residual faint diffuse emission from the Galactic foreground. This results in spurious detections of polarized emission at low levels. The effect can be seen in Fig. 6 as blue dots that rise above the detection threshold at peak flux densities below $\sim$100 μJy bm^{-1}. These sources have very high fractional polarization. To remove them we have applied a filter in total flux density and fractional polarization. This results in 216 polarization detections in the merged XMMLSS source list.

4.4 Polarization and Faraday depth measurement

Following the analysis to measure detections of polarized emission. The Faraday synthesis was redone for each source in fractional polarization. For this purpose the observed (before primary beam correction) Stokes I peak flux spectrum over the full 880–1680 MHz band is fit by a power-law function of the form

$$I(\nu) = I_o \left(\frac{\nu}{\nu_o}\right)^{\alpha + C \ln(\nu/\nu_o)} . \quad (12)$$

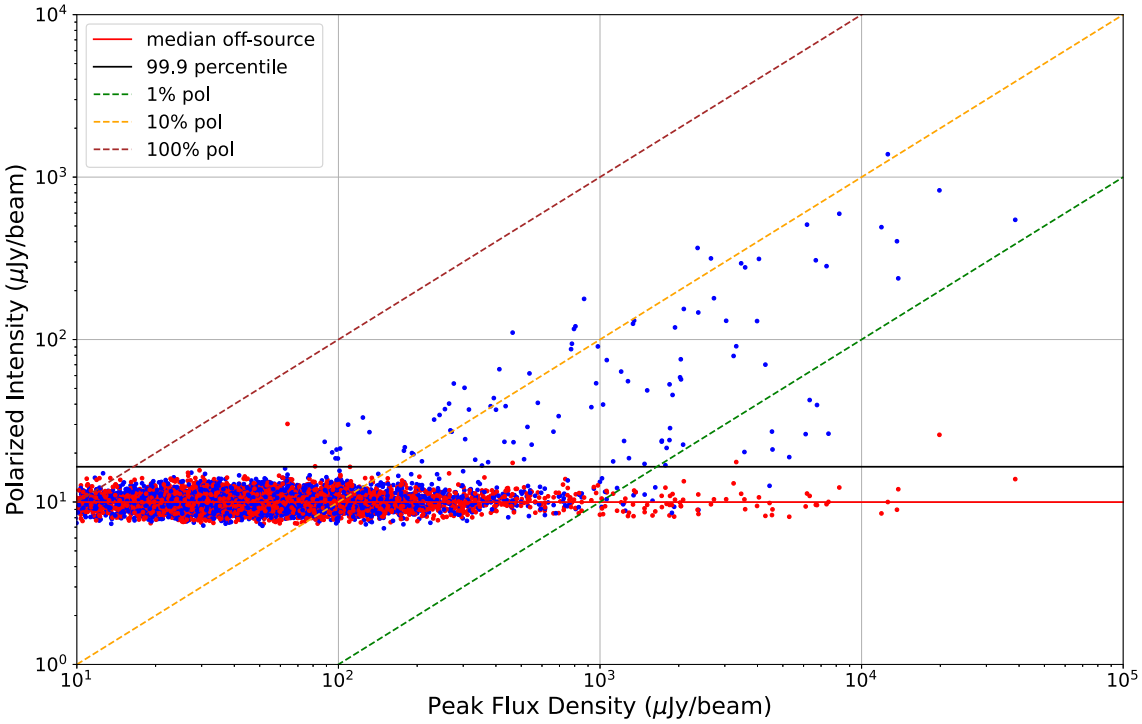

Figure 5. Polarized intensity of the maximum of the RM synthesis spectra for the on-source (blue dots) and off-source (red dots) positions plotted against the peak total intensity for each source. This plot is for the COSMOS field. The diagonal dashed lines represent lines of constant fractional polarization of 1, 10, and 100 per cent. The horizontal red line is the median value of the off-source spectral peaks. The horizontal black line shows the 99.9 percentile of the off-source spectral peaks at 16.5 μJy bm^{-1}.

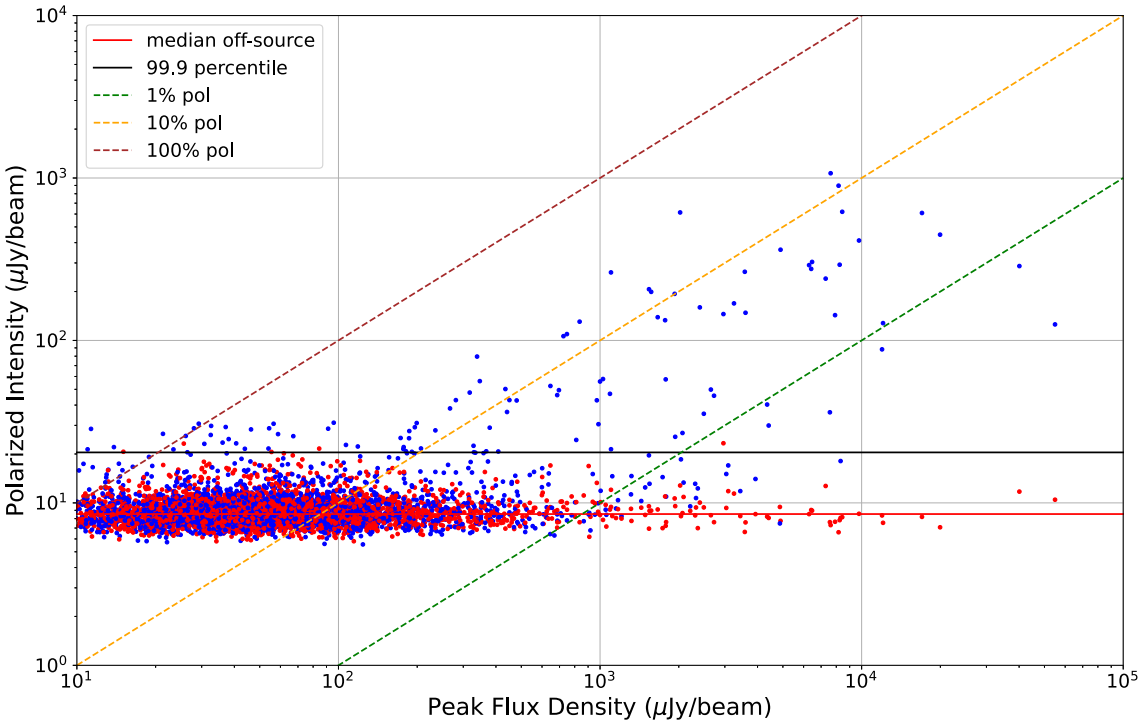

Figure 6. As in Fig. 5, but for XMMLSS_14. Note the clustering of blue dots are very faint peak total intensity with very high percentage polarization that are not seen in the COSMOS data. These points arise due to the presence of faint, structured diffuse emission from the Galactic foreground in the XMMLSS fields.

Table 3. Polarized intensity detection thresholds and number of detected polarized sources in each MIGHTEE early science field.

Field	Total sources ($r < 0.5°$)	Detection threshold (μJy bm^{-1})	Detected
XMMLSS_12	3695	27.4	121
XMMLSS_13	3368	31.0	89
XMMLSS_14	3405	27.4	143
COSMOS	3840	16.5	108

The quantity P_j in equation (9) is replaced by

$$p_j = \frac{(Q - Q_{\rm bkgd})_j - i(U - U_{\rm bkgd})_j}{I(\nu_j)}. \quad (13)$$

and the weights become

$$w_j = \left(\frac{I(\nu_j)}{\sigma_{QU_j}}\right)^2. \quad (14)$$

For each source, the amplitude (per cent) and the position of the dominant component of the Faraday depth spectra was recorded. The effective frequency of the measurements is taken as the weighted mean frequency of the channels used. The uncertainty on Faraday depth can be calculated as

$$\Delta_\phi = \frac{\delta\phi}{2|P_{\rm peak}|/\sigma_{\rm snyth}}, \quad (15)$$

where $\delta\phi$ is FWHM of the RM transfer function, $P_{\rm peak}$ is the peak amplitude and $\sigma_{\rm synth}$ is the noise in the RM synthesis spectrum (Brentjens & de Bruyn 2005), measured as the RMS of the real component of the off-source spectrum.

For polarization detections we also derived Faraday depth values for the strongest component in each spectrum derived using the QU-fitting technique on the background-subtracted QU data.[3] The recovered rotation measure for each source is represented by a maximum-a-posteriori (MAP) expectation value obtained using MCMC optimization of a single Faraday-thin component model. In each case the MAP value was obtained using an MCMC with a randomly initialized burnin of 5000 samples per chain, followed by a production run of 10 000 samples initialized from the maximum-likelihood (ML) value of the burnin. The MCMC uses uniform priors in the range $0 < P_0 < 100$ per cent, $-1000 < \phi_0 < +1000$ rad m^{-2}, and $-\pi/2 \leq \chi_0 < \pi/2$ radians. Following the burnin, the χ_0 prior is relocalised to cover π radians around the ML initialization point. MCMC convergence was assessed using the autocorrelation length of the chains; a burn-in of 5 times the autocorrelation length was discarded and chains were thinned by a factor of 15 in order to calculate final posterior distributions. Posterior uncertainties at a level of 1σ are provided for MAP estimates. An example of the posterior distributions obtained from QU-fitting is shown in Fig. 7 for the XMMLSS source ID 6607. The relationship between the RM estimates recovered from QU-fitting and those measured directly from the Faraday depth spectra is illustrated in Appendix B.

Fig. 8 shows the distribution of Faraday depth of the dominant Faraday depth spectral component for each of the polarized sources for the COSMOS and XMMLSS data. The median value of the COSMOS $*$Faraday depth is 1.03 rad m^{-2}, with a RMS estimated from the Median Asbolute Deviation of 6.60 rad m^{-2}. For *XMM*-LSS the median is signficantly higher at 8.24 rad m^{-2} but with an essentially identical RMS of 6.56 rad m^{-2}. The enhanced median Faraday depth of *XMM*-LSS is due to the Galactic foreground Faraday screen.

[3] https://github.com/as595/QUFitting

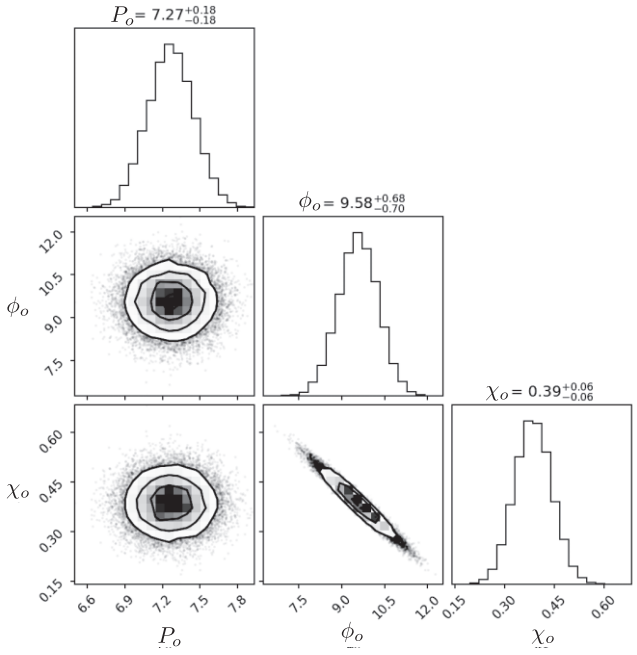

Figure 7. Posterior probability distribution from QU-fitting of source ID 1412 in the XMMLSS field. Parameters are: P_0, the polarization percentage; ϕ_0, the Faraday depth; and χ_0, the intrinsic polarization angle. Contours show confidence intervals from 1σ to 3σ.

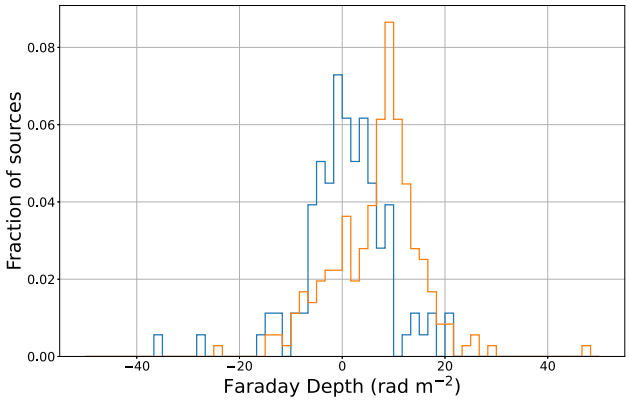

Figure 8. Distribution of Faraday depth of the dominant Faraday depth component for polarized sources in XMMLSS (blue) and COSMOS (orange).

Hutschenreuter et al. (2022) created an interpolated all-sky image of the foreground Galactic Rotation Measure (GRM) based on a compilation of data sources with an average density of about 1 RM per square degree. The median values of the MIGHTEE Faraday depths are in general agreement with the mean values over each field from Hutschenreuter et al. (2022) of -0.5 ± 7.6 for COSMOS and 6.7 ± 5.7 for *XMM*-LSS.

More local estimates of GRM can also be made for the area around each MIGHTEE source, i, using the polarized sources that are within a radius, R, from that source. We take the median of all sources within that radius to estimate the local median RM, $\Phi_{i,R}$. The local uncertainty for each estimate, $\Delta_{\Phi_{i,R}}$, is calculated from the median absolute deviation of the selected sources.

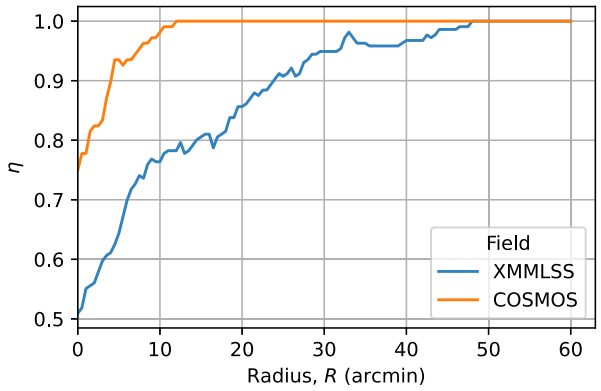

Figure 9. The fraction, η, of MIGHTEE-POL Galactic RM estimates which lie within 1σ of the GRM value from Hutschenreuter et al. (2022), as a function of the radius, R, used to estimate the local GRM.

We define a quantity η:

$$\eta = \frac{1}{N}\sum_{i=1}^{N} \begin{cases} 1 & \text{if } \left|\Phi_{i,R} - \Phi_{i,\mathrm{H}+}\right| < \sqrt{\Delta^2_{\Phi_{i,R}} + \Delta^2_{\Phi_{i,\mathrm{H}+}}} \\ 0 & \text{else.} \end{cases}, \quad (16)$$

where $\Phi_{i,\mathrm{H}+}$ and $\Delta_{\Phi_{i,\mathrm{H}+}}$ are the value of the GRM and GRM error at the position of source i from Hutschenreuter et al. (2022), and N is the number of sources in a given field. Conceptually, η is the fraction of local GRM values that are within 1σ of the current literature GRM values.

We use η as a function of the radius, R, with which we select sources to include in the median value to highlight the convergence of the local GRM estimates to the lower resolution GRM estimates from Hutschenreuter et al. (2022) as R increases. This is illustrated in Fig. 9, which shows a clear convergence of both fields to the literature values as R approaches 1 degree. Deviations from the literature value for smaller values of R imply significant angular structure of the foreground RM on sub-degree scales. This effect is stronger in *XMM*-LSS where the average foreground is larger compared to COSMOS. Studies that rely on data sampled on degree scales to remove foreground RM estimates will suffer significant uncertainty. A more detailed analysis these previously unseen Galactic RM structures will be presented in future work.

5 SPECTRAL INDEX

Equation (12) was used to fit the total intensity spectrum for all sources to derive an internal spectral index. Before fitting the peak total intensities in each channel are corrected for the primary beam variation in direction and frequency using the katbeam python module[4], which uses the circularly symmetric cosine-squared formulation described in Mauch et al. (2020).

For polarization detections a polarization spectral index, β is calculated by fitting a power law $p(\lambda) \propto \lambda^{\beta}$ to the per cent polarization $p(\lambda)$. Before fitting, following George, Stil & Keller (2012), the $p(\lambda)$ from equation (13) for each channel is bias corrected using σ_{QU},

$$p(\lambda_i)_{\mathrm{bias}} = \sqrt{p(\lambda_i)^2 - 2.3\sigma^2_{QU_i}}. \quad (17)$$

Sources with $\beta < 0$ are 'depolarized' with lower fractional polarization at lower frequencies. This behaviour is generally attributed

[4]https://github.com/ska-sa/katbeam

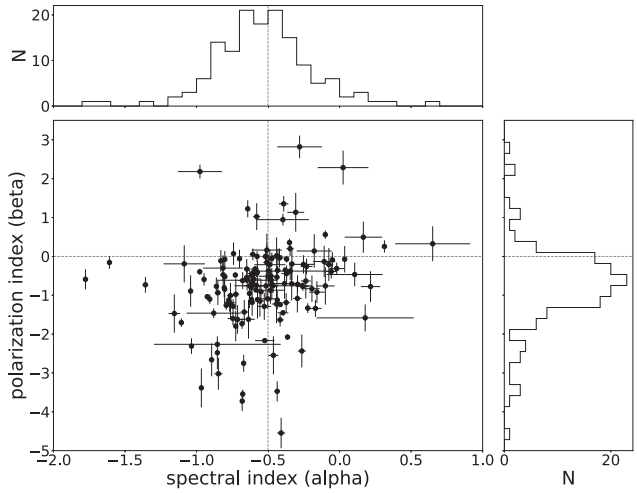

Figure 10. Fractional polarization spectral index, β, versus total intensity spectral index, α, for 143 polarized sources with errors $\sigma_\alpha < 0.3$ and $\sigma_\beta < 0.5$. The top and side panels show the distributions in α and β. The vertical and horizontal dashed lines divide the plot into quadrants at $\alpha = -0.5$ and $\beta = 0$.

to disordered magnetic fields or to internal or external Faraday depolarization. A overview of spectral models of depolarization processes can be found in Farnes, Gaensler & Carretti (2014), who compiled and modelled the polarized spectral energy distributions derived from the literature for 951 strong sources. The polarized flux limit of the Farnes, Gaensler & Carretti (2014) is based on the NVSS RM catalogue (Taylor, Stil & Sunstrum 2009), about 3 mJy at 1400 MHz. Sources with $\beta > 0$ are so-called 'repolarized' sources, with fractional polarization increasing at longer wavelengths.

Due to the limited frequency range (880–1380 MHz) for the Faraday synthesis, the derivation of β has high uncertainty for the faintest polarized sources. In Fig. 10, we plot β versus the total intensity spectral index α for 143 polarized sources for which the 1σ error on β is less than 0.5 and the error on α is less than 0.3. The figure shows a similar result to the findings of Farnes, Gaensler & Carretti (2014; see their fig. 7). There is a trend of stronger depolarization towards sources with more negative spectral index. Repolarization is observed for 13 per cent of the sources, and predominantly for objects with flatter spectral index. The relationship between α and β emphasizes the conclusion that depolarization and repolarization are intrinsic properties of the emitting sources, as opposed to external effects.

6 REDSHIFTS

The radio sources were cross-matched with photometric and spectroscopic redshift data from Adams et al. (2021) and Hatfield et al. (2022). Additional spectroscopic redshifts from Vaccari (2022) were cross-matched.

Each redshift catalogue was cross-matched with the radio source catalogue utilising the python astropy function `match_coordinates_sky`. The catalogues are cross-matched within a matching radius $d_{\rm match}$ depending on radio source position uncertainties $\sigma_{\rm ra}$ and $\sigma_{\rm Dec.}$ via $d_{\rm match} = x_\sigma \cdot d_\sigma$ where

$$d_\sigma = \sqrt{\sigma_{\rm ra}^2 + \sigma_{\rm dec}^2 + 2\sigma_{\rm opt}^2} \quad . \tag{18}$$

The source positions uncertainties of the redshift catalogues, which based on optical observations, are assumed to be $\sigma_{\rm opt} = 0.3$ arcsec.

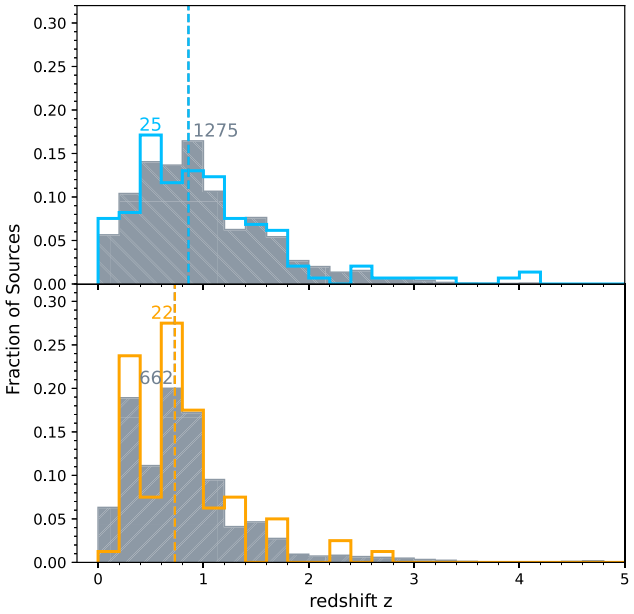

Figure 11. Redshift distribution for *XMM*-LSS (top) and COSMOS (bottom). The plot shows the fraction of sources against the best redshift estimate. For *XMM*-LSS 7753 radio sources have corresponding redshifts (top grey histogram) of which 216 are detected in polarized emission (blue). In the COSMOS field 3308 radio sources have corresponding redshifts (bottom grey histogram) of which 81 show polarized emission (orange). The dashed lines indicate the median redshift for each distribution; it is virtually identical between the polarized sources and the total population in each field. The number on top of the highest bin shows the source count in that bin.

The scaling factor x_σ was calculated to maximize reliability and completeness by performing a statistical matching analysis similar to the approach of Farnes, Gaensler & Carretti (2014) and Mauch & Sadler (2007). The actual match count is compared to the match count between the same catalogues with randomized source positions as a function of x_σ to determine the largest matching radius at which match counts still differ from match counts with randomized positions. At that radius, we estimate the completeness by counting the first neighbour matches as well as the fraction of spurious source associations by counting the matches of the second neighbour matches. The Adams et al. (2021) catalogue has a high source density. We used $x_\sigma = 1.5$, resulting in matches for 81.1 per cent (3.3 per cent spurious) of the radio sources in *XMM*-LSS and 81.4 per cent (5.3 per cent spurious) in COSMOS. For Vaccari (2022) a value of $x_\sigma = 4.5$ provided matches for 40.6 per cent (6.0 per cent spurious) of the radio sources in *XMM*-LSS and 56.4 per cent (10.1 per cent spurious) in COSMOS.

Fig. 11 shows the redshift distribution for all redshift-associated sources in *XMM*-LSS and COSMOS. Following Duncan (2022), we exclude photometric redshifts $z_{\rm phot}$ with very high uncertainties

$$\sigma_z/(1 + z_{\rm phot}) > 0.2 \, . \tag{19}$$

This affects 849 sources in *XMM*-LSS and 279 in COSMOS. Of the 324 detected polarised radio sources, 227 have associated redshifts, see Table 4 for details. The redshift distribution of the polarized detections are shown as the solid lines in Fig. 11. The polarized sources are seen at all redshifts and follow the same redshift distribution as the total radio source population. The median redshifts for both populations in *XMM*-LSS and COSMOS are virtually

Table 4. Number of polarized sources with spectroscopic and photometric redshift for *XMM*-LSS and COSMOS.

Field	Total	Spectroscopic z	Photometric z
XMM-LSS	146	92	54
COSMOS	81	69	12
Total	227	161	66

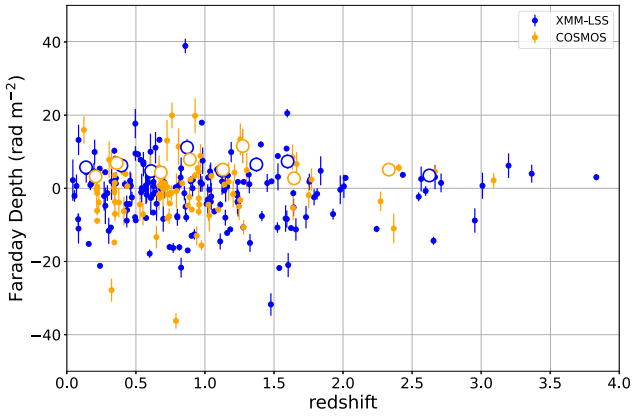

Figure 12. Faraday depth of the dominant Faraday component, with Galactic foreground estimate removed, against redshift for *XMM*-LSS (blue) and COSMOS (orange). Large open circles are the standard deviation of the Faraday depths in redshift bins. Bin widths are $\Delta z = 0.25$ out to $z = 1.75$. The final bin contains all sources with $z > 1.75$.

identical. *XMM*-LSS: $z_{\rm med} = 0.8576$, $z_{\rm med,\,pol} = 0.8585$; COSMOS: $z_{\rm med} = 0.7280$, $z_{\rm med,\,pol} = 0.7292$.

To reduce the effect of the foreground GRM on the Faraday depths, we define an average Faraday depth for all sources within a given pointing, and subtract the average from each source in that pointing. Fig. 12 shows the foreground-removed Faraday depth of the dominant Faraday synthesis component for each polarized sources as a function of redshift. Because of the wide bandwidth and high sensitivity of the MIGHTEE observations, the error on the measurement of Faraday depth is quite low, from less than 1 to a few rad m^{-2}. The scatter in the redshifts is thus due to a combination of scatter in the intrinsic Faraday depth of the radio sources, or small-scale spatial variation in the Galactic foreground screen. The large open circles in Fig. 12 show the standard deviation of the Faraday depths in redshift bins. The bin width is $\Delta z = 0.25$ out to $z = 1.75$. The final bin contains all sources with $z > 1.75$. To reduce the impact of outliers, the standard deviations are estimated from the median absolute deviation. There is no evidence of a trend in the magnitude of the standard deviation of the Faraday depths with redshift. The average standard deviation is 5.9 ± 2.7 for COSMOS and 6.3 ± 2.2 for *XMM*-LSS. The slightly larger value for *XMM*-LSS may reflect an increased contribution from scatter in the GRM, as suggested in Fig. 9.

Hammond, Robishaw & Gaensler (2013) catalogued redshifts for 4003 sources from the Taylor, Stil & Sunstrum (2009) NVSS 1.4 GHz RM catalogue. While the typical error on the NVSS RMs is much larger (10–20 rad m^{-2}), Hammond, Robishaw & Gaensler (2013) also found no evidence for redshift evolution in RMs corrected for the Galactic foreground. Using very precise RM from the LOFAR Two-metre Sky Survey Data Release 2 (Shimwell et al. 2022), Pomakov et al. (2022) measured an average difference in $|RM|$ of 1.79 ± 0.09 between pairs of objects at different redshifts that share the same line of sight to within 30 arcmin. This difference is independent of the redshift difference between the pairs. The structure in Galactic RM seen in our data imply that at least some or all of this signal may arise from differential GRM on small scales.

Bernet, Miniati & Lilly (2012) similarly found no evidence for an increase in the dispersion of Faraday depths with redshift using the Taylor, Stil & Sunstrum (2009) data. This is despite detecting an increase of dispersion from Faraday depths derived at 5 GHz. To account for this difference, Bernet, Miniati & Lilly (2012) model the observed RM as the sum of the foreground GRM and a contribution from an inhomogeneous Faraday screen at the source. The polarized emission from the source is described as

$$p = p_o\left(f_c \exp(-2\sigma_{\rm RM}^2(1+z)^{-4}\lambda^4) + (1 - f_c)\right). \quad (20)$$

Here f_c is the covering factor of the screen over the source, $\sigma_{\rm RM}$ is the Faraday dispersion of the screen and λ is the radiation wavelength. As shown by Bernet, Miniati & Lilly (2012) for low frequencies the portion f_c of the polarized flux at source that propagates through the Faraday screen is depolarized. We have carried out some Monte Carlo simulations of this model as a function of redshift and find that the partial Faraday screen at source introduces additional scatter at low redshifts. The scatter is reduced at high redshift due to the shorter wavelength of the radiation at source. This effect runs counter to the expected increase with redshift in the magnitude of RM and may obscure its detection with low-frequency observations.

7 CATALOGUES AND DATA

Catalogues of spectra-polarimetric data and Faraday synthesis result are provided for each source as fits tables. The following four files are provided for each of COSMOS and *XMM*-LSS.

`<Field>_pybdsf.fits`: contains the pyBDSF total intensity source list for all sources within 0.5° of the <field> image centre. Source parameter columns are as described in the pybdsf documentation[5]

`<Field>_allsources.fits`: contains spectral and Faraday synthesis results for all sources. The columns are:

(i) the source ID cross-referenced to `<Field>_pybdsf.fits`;
(ii) the RA and Dec., with errors;
(iii) the integrated flux density from pyBDSF corrected for the primary beam, with error;
(iv) the in-band peak total intensity spectral index and error;
(v) the in-band peak total intensity spectral curvature term and error;
(vi) the raw and bias-corrected polarized intensity of the strongest component in the on-source fractional polarization Faraday Depth spectrum;
(vii) the P, Q, U fractional polarization of the strongest component in the on-source fractional polarization Faraday depth spectrum;
(viii) the Faraday depth of the strongest component in the on-source fractional polarization RM synthesis spectrum, with error;
(ix) polarized intensity and Faraday Depth of the peak of the off-source RM synthesis spectrum;
(x) the effective frequency of the Faraday synthesis;
(xi) 'best_z_mightee': The best redshift estimate.
(xii) 'best_z_mightee_err': Photometric redshift uncertainty.

[5]https://pybdsf.readthedocs.io/en/latest/

(xiii) 'best_z_mightee_origin': Descriptor for the origin of the redshift estimate. 'phot_z' and 'spec_z' for photometric and spectroscopic redshift from Adams et al. (2021) and Hatfield et al. (2022); 'ZBEST' for spectroscopic redshifts from Vaccari (2022).

`<Field>_poldetections.fits`: contains spectro-polarimetric parameters for all sources with detected polarized emission. Columns are:

(i) the source ID cross-referenced to the original pyBDSF catalogue;
(ii) the RA and Dec. coordinates with error from the pyBDSF catalogue;
(iii) the integrated flux density in the MFS image from pyBDSF corrected for the primary beam with error;
(iv) the in-band peak intensity spectral index (α) and error;
(v) the polarization index (β) with error;
(vi) the raw and bias-corrected polarized intensity of the strongest component in the on-source fractional polarization Faraday depth spectrum;
(vii) the P, Q, U fractional polarization of the strongest component in the on-source fractional polarization Faraday depth spectrum;
(viii) the median fractional Stokes V amplitude across the band;
(ix) the Faraday depth of the strongest component in the on-source fractional polarization RM synthesis spectrum with error;
(x) the effective frequency of the weighted fractional polarization RM synthesis spectrum (see equation 11);
(xi) the MAP expectation RM from QU-fitting, using the uniform priors described above;
(xii) the 1σ uncertainty (upper bound) on the MAP RM from QU-fitting derived from the posterior distribution;
(xiii) the 1σ uncertainty (lower bound) on the MAP RM from QU-fitting derived from the posterior distribution;
(xiv) 'best_z_mightee': The best redshift estimate;
(xv) 'best_z_mightee_err': Photometric redshift uncertainty;
(xvi) 'best_z_mightee_origin': Descriptor for the origin of the redshift estimate. 'phot_z' and 'spec_z' for photometric and spectroscopic redshift from Adams et al. (2021) and Hatfield et al. (2022); 'ZBEST' for spectroscopic redshifts from Vaccari (2022).

`<Field>_spectra.fits`: contains primary beam corrected Stokes spectra for all sources. Columns are:

(i) Source ID
(ii) Frequencies of the channels
(iii) The primary beam correction for each channel
(iv) Stokes I intensity spectrum
(v) The Stokes I intensity model spectrum
(vi) The Stokes Q intensity spectrum
(vii) The Stokes U intensity spectrum
(viii) The Stokes Q background intensity spectrum ($Q_{\rm bkgd}$)
(ix) The Stokes U background intensity spectrum ($U_{\rm bkgd}$)
(x) The per channel average Q, U noise (σ_{QU})

Because the number of frequency channels differs among the three *XMM*-LSS pointings, individual `<Field>_spectra.fits` files are provided for each of XMMLSS_12, XMMLSS_13, and XMMLSS_14.

7.1 Astrometry and flux scale

7.1.1 Astrometry

The astrometric offsets were determined by comparing the catalogue source positions with source positions from catalogue of compiled optical and infrared data by Adams et al. (2021). We find significant systematic offsets in the radio coordinates in all fields. The offsets are the same within errors for all observations of a particular field but different for *XMM*-LSS and COSMOS, which suggests the offsets are due to small systematic errors in the array geometry. The visibility data from the individual observations of each field were thus combined in uncorrected form and the astrometric corrections per field were derived from the images of the combined visibilities. Table 5 lists the astrometric shifts for each field. These are the median difference in RA and Dec. for all sources with a match in Adams et al. (2021).

Table 5. Systematic astrometric offsets of the MIGHTEE-pol early science fields. All images and catalogues have been corrected to remove these offsets.

Pointing	ΔRA (arcsec)	ΔDec (arcsec)
XMMLSS_12	0.2743 ± 0.0008	0.5261 ± 0.0008
XMMLSS_13	0.2566 ± 0.0008	0.5705 ± 0.0009
XMMLSS_14	0.2547 ± 0.0008	0.5725 ± 0.0009
COSMOS	0.2657 ± 0.0010	0.1420 ± 0.0010

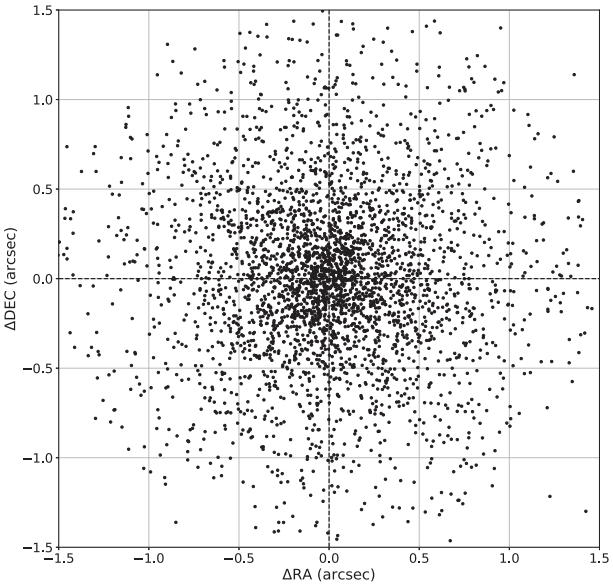

Figure 13. Position differences in RA and Dec. for sources in *XMM*-LSS against the optical positions of Adams et al. (2021) after correcting for the systematic astrometric error in Table 5.

The image and catalogue data sets have been corrected for these astrometric errors. An example bull's eye plot, for the XMMLSS_14 field, after correction is shown in Fig. 13.

7.1.2 Flux scale

The flux scale was examined by comparing the catalogue source fluxes with the fluxes from the MIGHTEE Continuum source catalogues of the same fields (Heywood et al. 2022). The Heywood et al. images have centre frequency at 1.284 GHz, essentially the same as our MIGHTEE-pol images. We find an overall difference of about 7 per cent in the source integrated flux densities for the XMMLSS fields, and a difference of 10 per cent for the COSMOS pointing. In both cases, the flux densities in MIGHTEE-Pol are lower than the corresponding MIGHTEE-Cont measurements. Fig. 14 shows

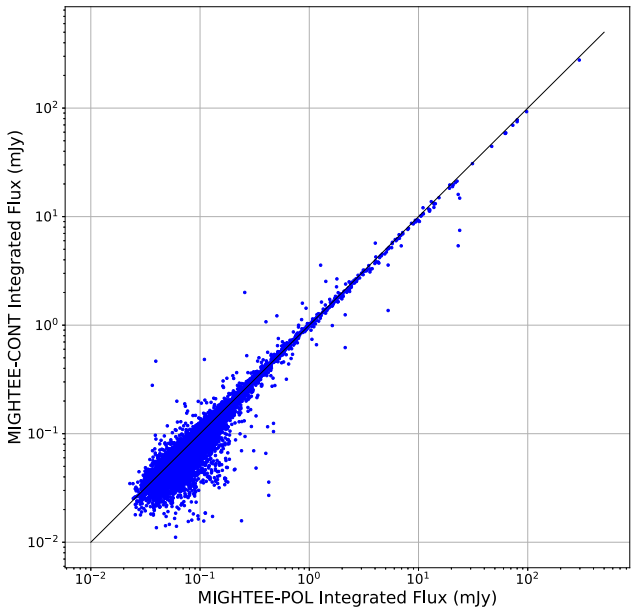

Figure 14. Flux comparison between these data and the MIGHTEE-Cont continuum data release (Heywood et al. 2022) over all the XMMLSS fields. The solid line is a linear fit to the data. We see 6.5 per cent lower flux density in this case, and ∼10 per cent in the case of COSMOS. The exact reason for this flux scale discrepancy is unknown at the moment, so we have elected to not correct our flux density scales to match MIGHTEE-cont.

the flux–flux plot of MIGHTEE-Pol integrated flux density versus MIGHTEE-Cont.

The MIGHTEE Continuum catalogue for the comparison were generated at Briggs robust = 0.0, whereas the MIGHTEE-polarization images are generated at robust = −0.5. The lower robust for the MIGHTEE-continuum leads to a larger synthesized beam and a higher brightness sensitivity. The MIGHTEE-continuum images also include visibilities at long baselines over the frequency channels that are removed in our data. The MIGHTEE-continuum thus uses about 800 MHz of bandwidth, compared to 585 MHz for our data.

While we do not expect these effects to cause as much as a 10 per cent change in measured source flux, these plus differences in the calibration and imaging processes that may explain the offset. We have elected not to apply any correction for the overall flux scaling. Fractional polarization and Faraday synthesis results are not affected by systematics in flux scale. The catalogues of source polarization in this paper will be accurate to within the limitations of leakage as discussed in Section 4.2.

ACKNOWLEDGEMENTS

The MeerKAT telescope is operated by the South African Radio Astronomy Observatory, which is a facility of the National Research Foundation, an agency of the Department of Science and Innovation. This work was carried out using the data processing pipelines developed at the Inter-University Institute for Data Intensive Astronomy (IDIA) and available at https://idia-pipelines.github.io. IDIA is a partnership of the University of Cape Town, the University of Pretoria, the University of the Western Cape. We acknowledge the use of the ilifu cloud computing facility – www.ilifu.ac.za, a partnership between the University of Cape Town, the University of the Western Cape, the University of Stellenbosch, Sol Plaatje University, the Cape Peninsula University of Technology, and the South African Radio Astronomy Observatory. The Ilifu facility is supported by contributions from the Inter-University Institute for Data Intensive Astronomy, the Computational Biology division at UCT, and the Data Intensive Research Initiative of South Africa (DIRISA).

8 DATA AVAILABILITY

The raw MeerKAT visibilities for which any proprietary period has expired can be obtained from the SARAO archive at https://archive.sarao.ac.za. The catalogues and images are available at the MeerKAT science archive at https://doi.org/10.48479/tedr-jf87, and on the public data repository of the IDIA science gateway at gateway.idia.ac.za.

REFERENCES

Adams N. J., Bowler R. A. A., Jarvis M. J., Häußler B., Lagos C. D. P., 2021, MNRAS, 506, 4933
Asad K. M. B. et al., 2021, MNRAS, 502, 2970
Bernet M. L., Miniati F., Lilly S. J., 2012, ApJ, 761, 144
Brentjens M. A., de Bruyn A. G., 2005, A&A, 441, 1217
Briggs D., 1995, Bulliten of the American Astronomical Society. vol. 27. American Astronomical Society, p.1444
Duncan K. J., 2022, MNRAS, 512, 3662
Farnes J. S., Gaensler B. M., Carretti E., 2014, ApJS, 212, 15
George S. J., Stil J. M., Keller B. W., 2012, PASA, 29, 214
Hales C. A., 2017, AJ, 154, 54
Hammond A. M., Robishaw T., Gaensler B. M., 2013, A New Catalog of Faraday Rotation Measures and Redshifts for Extragalactic Radio Sources
Hatfield P. W., Jarvis M. J., Adams N., Bowler R. A. A., Häußler B., Duncan K. J., 2022, MNRAS, 513, 3719
Heald G. et al., 2020, 53 Galaxies, 8
Heywood I. et al., 2022, MNRAS, 509, 2150
Hutschenreuter S. et al., 2022, A&A, 657, A43
Jarvis M. et al., 2016, in Taylor A.R., Camilo F., Leeuw L., Moodley K., eds, MeerKAT Science: On the Pathway to the SKA. Proceedings of Science, p. 6
Jonas J., Team MeerKAT , 2016, in Taylor A.R, Camilo F., Leeuw L., Moodley K., eds, MeerKAT Science: On the Pathway to the SKA. Proceedings of Science, p. 1
Mauch T., Sadler E. M., 2007, MNRAS, 375, 931
Mauch T. et al., 2020, ApJ, 888, 61
Pomakov V. P. et al., 2022, MNRAS, 515, 256
Rau U., Cornwell T. J., 2011, A&A, 532, A71
Sekhar S., Jagannathan P., Kirk B., Bhatnagar S., Taylor R., 2022, ApJ, 163, 87
Shimwell T. W. et al., 2022, A&A, 659, A1
Taylor A. R., Stil J. M., Sunstrum C., 2009, ApJ, 702, 1230
Taylor R. et al., 2015, PoS, AASKA14, 113
Vaccari M., 2022, The Spitzer Spectroscopic Data Fusion—Merged Spectroscopic Redshift Catalogs in Spitzer Fields. zenodo

APPENDIX A: FARADAY COMPLETENESS

We assess the completeness of the catalogued polarized source detections in Faraday depth using simulations. For 100 randomly selected lines of sight from each field, we use the recorded frequency channels to simulate the expected Stokes Q and U for a population of Faraday thin sources with a range of signal-to-noise ratios (SNR), where the SNR is determined by the individual per channel noise values. The Faraday depth and intrinsic polarisation angle for each simulated source are drawn from uniform distributions with $\phi_0 \sim \mathcal{U}(-200, +200)$ and $\chi_0 \sim \mathcal{U}(-\pi/2, +\pi/2)$, respectively. Completeness (and false-positive rate; FPR) is estimated based on the

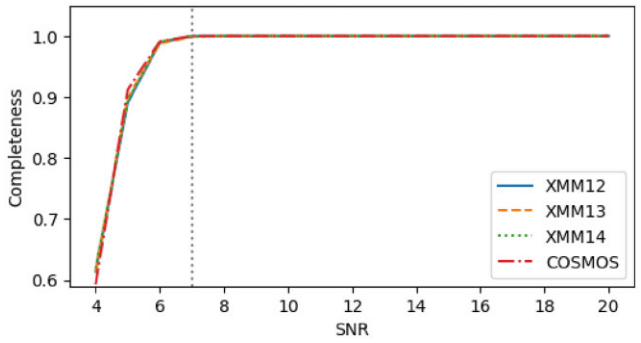

Figure A1. Faraday completeness.

Table A1. Faraday completeness [Per cent].

Field	σ_ϕ	SNR 4	5	6	7	8	9	10
XMM12	2.31	61.4	89.1	98.9	100	100	100	100
XMM13	2.53	61.4	89.8	98.8	99.9	100	100	100
XMM14	2.41	61.9	89.5	99.1	99.9	100	100	100
COSMOS	2.97	59.3	91.2	99.1	100	100	100	100

number of peaks detected in the absolute polarization as a function of Faraday depth above a level of $4\,\sigma$ (see Section 4.3), where σ is the rms noise in Faraday depth. Detections are considered to be true positives (TP) when the recovered Faraday depth of the peak lies within one FWHM of the RMTF centred on the input Faraday depth value; detections are considered to be false positives (FP) when their peak lies outside this range and has an absolute polarization greater than that of any true positive present in the data (or greater than the detection threshold in the case that no true positive is detected). Faraday completeness as a function of SNR is shown for each field in Fig. A1 and summarized in Table A1. The false positive rate in percent is listed as a function of SNR in Table A2. These results suggest that the polarization detections are complete above 7σ for all fields, equivalent to a flux density completeness limit of approximately 17.5 μJy beam^{-1}.

APPENDIX B: QU FITTING

A comparison of the RM values recovered using the peak of the Faraday depth spectrum versus those recovered by fitting directly to the Stokes Q and Stokes U data is shown in Fig. B1. It can be seen

Table A2. Faraday false positive rate [Per cent]. I have

Field	SNR 4	5	6	7	8	9	10
XMM12	7.2	3.1	1.1	0.0	0.0	0.0	0.0
XMM13	8.5	3.1	0.3	0.0	0.0	0.0	0.0
XMM14	6.5	2.8	0.1	0.0	0.0	0.0	0.0
COSMOS	6.5	2.3	0.7	0.2	0.0	0.0	0.0

visually that the recovered values are consistent within 1σ for all sources. Two sources within the COSMOS field show particularly high uncertainty associated with the RM values recovered from QU-fitting (ID 1277 and ID 2225). The Faraday depth spectra for both sources show significant secondary peaks and it is likely that the contribution of these components to the Stokes QU data is causing the posterior distributions to become broadened, resulting in larger marginalized uncertainties.

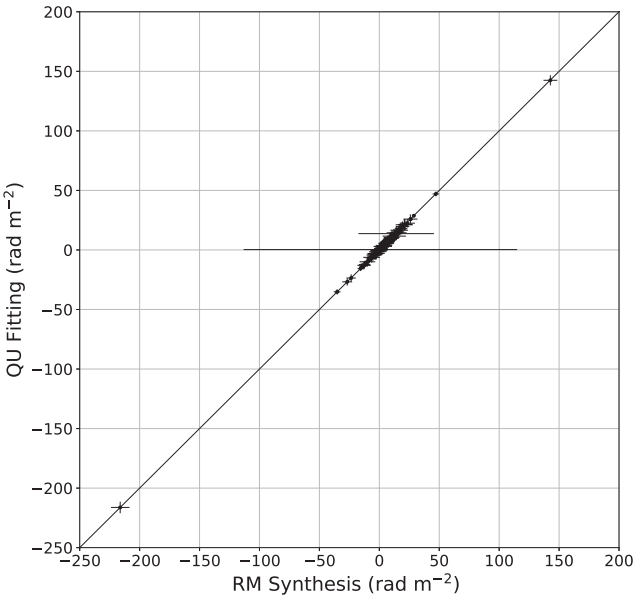

Figure B1. Distribution of catalogue RM values recovered directly from Faraday depth spectra and those recovered using the QU-fitting method for each field. Error bars show $1\,\sigma$ uncertainties as recorded in the MIGHTEE-POL early release catalogue, see Section 4.4 for details.

This paper has been typeset from a TEX/LATEX file prepared by the author.